Tracking the 3D atomic structures during thermal treatment and catalytic activity of individual Pt nanoparticles

Hoje Chun
Yonsei University
Joonhee Kang
Pusan National University
Dohun Kang
Northwestern University
Sung Jun Hong
Yonsei University
Junyoung Heo
Seoul National University https://orcid.org/0000-0003-4396-5200
Hyeongjin Cho
Soongsil University
Jaehyeon Heo
Soongsil University
Byung Hyo Kim
Soongsil University
Jungwon Park
Seoul National University https://orcid.org/0000-0003-2927-4331
Byungchan Han (bchan@yonsei.ac.kr)
Yonsei University https://orcid.org/0000-0002-2325-6733

Article

Keywords:

Posted Date: March 21st, 2022

DOI: https://doi.org/10.21203/rs.3.rs-1441062/v1

Abstract

To acquire a crystal-clear structure-performance relation for heterogeneous nanocatalysts, precise tracking of the structural evolution from the precursor to final product in the real time and space domain is important but also extremely challenging. In archetype preparation, thermal treatment is a crucial step for activation. Especially, for colloidally synthesized nanoparticles, the ligand detachment process to expose surfaces is completed with thermal treatment. Here, we track the three-dimensional atomic structural change of ligand-protected platinum nanoparticles under ligand detachment and thermal annealing processes. The structural transformation with time is shown by experimental decoupling and tracking of each atomic coordinate through molecular dynamics simulations with machine-learning potentials. Acquisition of structural data is integrated with a computational catalysis framework to identify a structure-activity correlation in the CO oxidation reaction. We find that colloidally synthesized platinum nanoparticles create unique atomic tensile strain and that varying the particle size tunes the ensemble effect of active sites.

Introduction

Heterogenous catalysis has been widely utilized in the majority of industrial processes to sustain human society, and nanoparticles (NPs) hold key roles in the success[1,2]. In modern society, NP catalysts are specifically targeted at efficiently producing green renewable fuels and powering electric vehicles to avoid environmental degradation induced by carbon-based energy systems. They are fabricated through manyfold reactions and post-processes before reaching their final form. This fact implies that the structures of NPs dynamically fluctuate in the chemical steps and are not static properties. More specifically, understanding the structural evolution of NP catalysts over various reaction steps and post-processes is essential, in which the thermal condition and reaction medium can be different from those for the precursor state. Typically, NP catalysts anchored on support materials are activated by thermal treatment to expose desired nanofacets and realize stability and quantum effects[3–5], whereby substantial deviation from the initial structures is introduced. Thus, regulating and tracking the structural evolution in the real time and space domain to extract a precise structure-activity map is important.

A colloidal method to prepare NPs as precursors overlaying support materials is emerging as a promising approach for functional catalyst design[6–8]. This is because effective control of complex parameters, such as the size and shape of NPs and spatial distribution on the support, is easier than with conventional methods. Moreover, the structural ensemble effect of NPs is easily engineered to facilitate the catalytic performance[9–11]. A key step in colloidal synthesis of NPs towards efficient heterogeneous catalysts is to expose desired surfaces for access by reaction intermediates. This is accomplished by ligand removal from supported colloidal nanocatalysts, *e.g.*, *via* UV-ozone treatment[12], a solvent washing step[13,14], an electrochemical step, and fast thermal treatment[4]. Then, typically, the exposed surfaces are activated by thermal annealing[6,15], whereby atomic positions are rearranged due to the high thermodynamic driving force. The structures produced by the processes show substantial heterogeneity

in atomic coordination environments or atomic strain[16]. The nonuniform structures in both single and ensemble NPs can influence the catalytic performance. Due to the dynamic nature of the surface atoms during the ligand removal process and thermal treatment, identifying the activated surface structure and a clear correlation with the catalytic activity is extremely challenging.

The atomic-level structure of an NP can be determined by several microscopy and spectroscopy techniques. For instance, fast characterization of active sites in platinum (Pt) NPs for carbon monoxide (CO) oxidation by infrared spectroscopy was demonstrated[17], and *in situ* field electron microscopy[18] was used to resolve the individual site reactivity for hydrogen oxidation. Our recent studies[19,20] demonstrated precise resolution of the three-dimensional (3D) atomic structure of colloidally synthesized Pt NPs in solution. Despite all these developments, experimental approaches have several limitations in directly resolving the structural evolution of catalytic NPs and in determining the structure-performance relationship at the atomic level. First-principles-based computational modelling, such as density functional theory (DFT) calculations, can be a good tool for this purpose. It can be effective for decoupling individual variables influencing catalytic reaction energetics, *i.e.*, ensemble (geometric), ligand (electronic), and strain effects[21–23]. However, most results from first-principles methods largely rely on ideal structural models, *e.g.*, uniform surfaces or magic-number NPs, neglecting the effects of surface nonuniformity and structural evolution in the reactive environments surrounding the NP catalysts.

In this work, we revealed the 3D atomic structural evolution of Pt NPs during the ligand detachment and subsequent thermal annealing process. The 3D atomic structures of the synthesized ligand-protected Pt NPs in solution were experimentally obtained with a 20 pm precision[19] and used as input for machine-learning-accelerated large-scale molecular dynamics (MD) simulations that directly elucidated atomistic behaviour of single NPs in the thermal annealing step. We demonstrate that the thermal energy drives NP structures to minimize the surface free energy. In addition, using the CO oxidation reaction, we acquired individual site contributions to the catalytic activity by revealing the kinetic coupling of adsorbates over heterogeneous atomic sites, which could not be captured by ideal modelling. Our results identify a clear correlation between individual atomic sites in the activated 3D surfaces and activity for the CO oxidation reaction.

Results And Discussion

Structural evolution in the ligand detachment process.

The overall experimental procedure is illustrated in Fig. 1a. Starting with the experimentally resolved 3D atomic structures of ligand-protected Pt NPs in liquid solution[19], MD simulations for the ligand detachment process followed by fast thermal annealing were performed for individual Pt NPs with varying sizes (NP1: 2.42 nm, NP2: 2.52 nm, NP3: 2.66 nm, and NP4: 2.92 nm). Tracking of the 3D atomic coordinates was carried out over the whole process to analyse the structural changes. Then, key features of the structures, *i.e.*, the generalized coordination number (GCN)[24] and strain, were fed into kinetic Monte

Carlo (kMC) simulations of the CO oxidation reaction. Last, the turnover frequency of individual particles was calculated to investigate the per-site activity.

One of the main bottlenecks in simulating the structure-property relation of the ligand detachment process in Pt NPs is a careful evaluation of the structural fluctuations. We addressed the issue by integrating a machine-learning neural network potential (NNP) with first-principles data of atomic energy to enable accurate and fast MD simulations. Various strategies have been applied to efficiently construct the NNP such as data augmentation[25] and active learning[26]. Our strategy is innovative in that it involves efficient construction of first-principles data by incorporating the experimentally reconstructed atomic configurations and defective NPs to describe various local atomic environments (Fig. 1b).

We generated local structural heterogeneity by using structures of experimentally resolved Pt NPs and highly defective Pt NPs at various intermediate steps acquired with first-principles calculations. To estimate the reliability of our approach, we compared the local atomic environments in ideal models and experimentally reconstructed structures (Fig. 1c). The ideal magic-number cuboctahedron consisting of 309 atoms shows only specific atomic environments, represented by the values of the radial (G^2) and angular (G^4) functions, with duplicated information (essentially core atoms), and this issue is still unresolved even with the addition of model structures. In contrast, the structural heterogeneity in the twenty structures of experimentally reconstructed Pt NPs provides much more densely mapped local configurations, which are fed into the feedforward neural network. Thus, we utilized the accelerated data collection method to make a training set for the NNP. Details of the first-principles data generation and the NNP training and validation results are provided in **Supplementary Sections 1 and 2**.

The structural evolution of individual Pt NPs during the ligand detachment process and thermal annealing was investigated *via* MD simulations with the constructed NNP. As shown in Fig. 1d, the total simulation time was 300 ps, in which the initial 100 ps corresponded to the thermal treatment with the ligand detachment process at 773 K, the next 100 ps to the quenching process to 303 K with a quenching speed of 4.7 K per ps, and the final 100 ps to equilibration at 303 K. The total energy of each NP becomes thermodynamically more stable as it undergoes the quenching process. We also observed that the larger the particle size is, the more stable the particle becomes (**Fig. S5**)[27,28]. The structural changes in NP3, representatively, show qualitative insights into the reduction of surface adatoms to form close-packed surfaces (Fig. 1d). The lattice parameters and averaged strain after the ligand detachment process indicate that the particle-wise structural heterogeneity decreases as Pt NPs approach the thermodynamic energy minima (**Fig. S6a**). However, the increase in the error magnitude reflects the flattened distributions of individual coordinates, which presumably signifies the diversified values of individual sites after the thermal treatment.

The temporal changes in the 3D atomic coordinates of NP3 obtained using MD simulations were further investigated. Figure 2a shows the changes in the fractions of the coordination number (CN), which is an index to evaluate the local atomic environments. We divided the atomic local environments into four classes in accordance with the CN[29]: CN = 12, CN = 10–11, CN = 9 – 7, and CN ≤ 6. Each environment

shows different behaviour with elapsed time, especially in the initial stage. The fractions of defective cores or subsurfaces of edges (CN = 10–11) do not fluctuate much, while other sites drastically change in the initial stage. The drastic change in the initial stage is mainly attributed to the ligand being instantly removed at the beginning of the simulation. The fraction of atoms with CN = 12, representing the face-centered cubic (fcc) lattice of the bulk, and that with CN ≤ 6, representing high-Miler-index facets, vertices, edges, or irregular islands of adatoms, decreased, whereas the fraction of atoms with CN = 9 − 7, representing (111) or (110) facets, increased. After the detachment process, the fcc lattice sites gradually recovered during the thermal annealing process. The surface atoms (CN ≤ 9) evolve in a way to minimize the surface energy, forming truncated octahedrons with (111) and (110) facets. The results for other Pt NPs were similar in that the number of surface adatoms initially binding ligands was reduced. The thermodynamic driving force of surface minimization can also be confirmed by the increase in the terrace (111) surface areas (Fig. 2b).

Local atomic arrangements were also analysed by the Voronoi tessellation method[30]. As shown in Fig. 2c, the distributions of the 25 most abundant Voronoi polyhedra (VPs) before and after the thermal treatments were obtained based on the Voronoi index $< n_3, n_4, n_5, n_6 >$, where n_i denotes the number of i-edged polygons. Before the treatment, most of the VPs are < 0, 0, 12, 0 > regular icosahedrons along with < 0, 11, 0, 0 > defective icosahedrons and < 0, 9, 0, 1 > polyhedral with multitetragonal surfaces. The major peaks for VPs before the treatment clearly indicate the single crystallinity of NP3. However, the crystallinity significantly decreases after the treatment (e.g., from 287 to 165 counts for < 0, 0, 12, 0>). Additionally, many VPs with low-edged polygons (n_3) appear, which indicates defective local atomic configurations. The defect identification by Wigner-Seitz analysis shows that all defects are on the surface (Fig. 2d).

As shown in Fig. 2e, the interatomic distances along the < 111>, < 100>, and < 110 > directions imply that the deviation increases as the atomic site moves away from the core of the NP, which is similar to the results of a previous study[19]. The distributions before and after the thermal treatment demonstrate that the interatomic distances along the < 111 > and < 110 > directions are rather similar (Fig. 2f). The distribution along the < 100 > direction at 300 ps with two peaks substantiates the surface energy difference among the (111), (110), and (100) surfaces in that adatoms preferentially penetrated into the (100) surface with the least stability and the smallest atomic packing factor. Our structural analyses consistently express the structural rearrangement of Pt NPs to minimize the surface energy induced by thermal energy during the ligand detachment and thermal treatment processes. The core crystallinity is mostly preserved, while surface reconstruction is unavoidable affecting the catalytic performance.

Structure-property relation with thermal treatment.

The chemical reaction energy in a single-component system is largely determined by structural features such as the local atomic coordination environment and strain[31,32]. Thus, we examined the GCN and atomic strain (**Supplementary Section 3**) at individual atomic sites of Pt NPs. The thermodynamic driving

force for surface energy minimization also induced drastic changes in both GCN and strain (**Fig. S7** and **S8**). Initially, all Pt NPs exhibited structural heterogeneity, especially surface atoms[29].

As the simulation time elapses, the density peaks for GCNs in the range of 4 to 6 increase, but those for high GCNs decrease. The increase in the density peaks for lower GCNs during the ligand detachment process implies the formation of, *e.g.*, (110) or higher Miller index, facets along with edges and vertices with GCN values in the range of 5.4 to 6.6, and 5.4 or lower, respectively. The vanishing peaks for very low GCNs indicate the penetration of adatoms into the surface lattice sites. The decrease in peaks for higher GCNs, similar to the CN results, signifies the reduction of core crystallinity, mainly due to the high processing temperature (773 K) of the ligand detachment process. The strain distributions of Pt NPs at the beginning also show the heterogeneity, with less correlation with the size after the process, in which NP2 has the lowest deviation of strain from equilibrium (**Fig. S6b**). One thing to note is that initially imposed tensile strains were preserved over the process, implying that colloidal methods can be beneficial for catalytic activity through an upshift of the *d*-band centre energy to enhance the binding affinity[33].

The structural features of the atomic sites were further analysed by decoupling the surface and core atoms (Fig. 3). Since catalytic reactions occur at the surface, the structural features of surface atoms are of interest. As shown in Fig. 3a, distinctive surface atom peaks (4.5 to 5 and 5.5 to 6 for edge atoms and high-index facets, respectively) are dominant for all Pt NPs, but the peak intensities vary. The core crystallinity is more preserved for larger-sized NPs, with higher peaks for GCNs in the range of 11 to 12. For all NPs, (111) facet formation ($6.6 < GCN < 7.5$) is clearly observed based on the colour-coded analysis, but some close- packed facets showed smaller GCNs. This is mainly attributed to the adatoms in the interstitial fcc lattice sites, which induced a void space between the surface and core. In contrast, the strain distributions of surface atoms show no distinctive peaks for all NPs (Fig. 3b). The major strain distributions initially resided in the range of 0 to 2 for all Pt NPs, but surface minimization effects resulted in high strain values (greater than $\pm$ 10) after the ligand detachment process. Colour-coded results also represent the predominant tensile strain over the surface atoms.

The change in average bond length was also computed as shown in **Fig. S9**. Core atoms suffer bond elongation, such as tensile atomic strain, but surface atoms suffer overall bond contraction. This is because the nearest neighbours of surface atoms consist of atoms in the same surface with a higher fraction (0.66) and atoms in the subsurface with a lower fraction (0.33) in general. Overall, the change in the structural features of individual Pt NPs after the ligand detachment process shows distinctive characteristics in that the ensemble of individual sites is magnified in terms of the GCN, while it is reduced in terms of the strain.

Individual site contributions to catalytic activity.

To investigate the ensemble effects of active sites on catalytic reactivity, we constructed microkinetic modelling and performed kMC simulations for CO oxidation in Pt NPs as a prototype catalysis

process[34,35]. Overall reaction energetics were adopted from the previous literature[16,36], but strain effects on the adsorption energy were revised by assigning individual atomic strain and site-dependent perturbations. Details of the reaction energetics and the kMC simulation are described in **Supplementary Section 4**.

Figure 4a shows the Arrhenius-type plot of the temperature-dependent turnover frequency (TOF) for different size Pt NPs. In general, the catalytic activity increases as the particle size increases, which is in accordance with a previous report[34]. Notably, such behaviour were not seen for modelled NPs[35]. To understand the peculiar size-dependent activity trend, we computed the fraction of surface atoms with respect to the total number of atoms and the fractions of active and inactive sites with respect to the number of surface atoms (Fig. 4b and **Fig. S11**). The surface atom fraction decreases with increasing particle size due to the reduction in the surface-to-volume ratio. The ensemble of active sites (TOF > $5{\cdot}10^4$ s^{-1} $site^{-1}$) is directly correlated with the activity of the particle, and the low fraction of inactive sites for larger particles indicates less kinetic hindrance. Interestingly, NP2 has a higher TOF than NP3 despite its smaller size.

The activities of ideal NPs (561 and 807 atoms) with similar sizes to NP1 to NP4 were computed. The results show that the NPs with high density peaks for the GCN have higher activity due to the ensemble effects of individual sites (**Fig. S12** and **Fig. S13**). To correlate the results of ideal NPs with those from NP1 to NP4, we compared the deviations in the number of atoms for each NP from that for the ideal NP models with (100) and (111) facets (**Fig. S14**). NP2 has a marginal deviation (0.01), while NP3 has a much higher deviation (0.10). We speculate that the extent of deviation can be a crucial factor; the closer the number of atoms of an NP is to that of the ideal model, the easier the NP can optimize towards the global minimum for facet formation. To summarize, the catalytic activity of NPs is dominated by the coupled effects of particle size and active site formation, increasing the individual site assembly.

To uncover how much different types of sites contribute to the total activity, we further analysed the TOF of Pt NPs through individual site analysis. First, we evaluated the effects of the GCN, as shown in Fig. 5a. In general, GCNs ranging from 4.8 to 5.5 yield high TOF, which indicates that the edge sites are the most reactive. In addition to the GCN, we considered the strain effect on the TOF of individual sites (Fig. 5b). We plotted the individual sites with TOF > 10^4 s^{-1} $site^{-1}$. The active sites were gathered in the region of low GCN (4.8 to 5.5) and tensile strain (5 to 10%). Notably, that the results for ideal model NPs are different (**Fig. S15**). Ideal model NPs exhibit catalytic activity for GCNs ranging from 4.8 to 5.5 and (111) facets, which is attributed to the kinetic coupling of adsorbates diffusing from the active sites[35]. However, surface structures are more heterogeneous in real conditions, in which the coupling effects are weakened, and thus the site responsiveness towards the target adsorbates becomes more important.

Conclusions

We demonstrated an experimental-computational framework to identify a structure-activity correlation with the thermal process in heterogeneous catalysis. It is based on an extremely reliable and high-

throughput structure database established by experimental analysis in the real time-space domain and computational tracking of each atomic coordinate under the thermal process. Interestingly, the surface minimization induced distinctive surface structures, which is dissimilar from ideal NP models. Experimentally resolved 3D atomic coordinates of Pt NPs enabled efficient generation of a first-principles database for machine-learning interatomic potentials and an understanding of catalytic activity with varying size. Structural evolution showed that ligand-protected Pt NPs preserve the tensile strain due to the ligand interaction even after the detachment process induced by thermal annealing. Using the CO oxidation reaction in colloidally synthesized Pt NPs, we characterized the individual site contributions to the overall catalytic activity, revealing that high-Miller-index or edge sites with tensile strain can be beneficial for the CO oxidation reaction. Our approach can be further developed to incorporate the support material effect on the catalytic activity.

Methods

The DFT structure-energy data set to train the potential energy surface of Pt was calculated using the Vienna *ab-initio* simulation package (VASP)[37-39]. The projector augmented wave[40] pseudopotential was used, and the generalized gradient approximation with Perdew-Burke-Ernzerhof (PBE) functional[40] was employed to describe the exchange-correlation energy. The cutoff energy for the plane-wave basis set was set to 400 eV. To train the atomistic potentials, we utilized the Behler-Parrinello high-dimensional neural NNP method[41] to determine the energy according to the local geometric motif within the cutoff radius of the reference atom as implemented in the Atomistic machine-learning package (Amp)[42]. The atom-centred symmetry functions (radial G^2 and angular G^4) based on the cutoff function (f_c) were used to represent the local environments.

$$f_c(R_{ij}) = \begin{cases} 0.5 \times \left[\cos\left(\frac{\pi R_{ij}}{R_c}\right) + 1\right] & for\ R_{ij} \le R_c \\ 0 & for\ R_{ij} > R_c \end{cases} \qquad (1)$$

R_{ij} is the interatomic distance between reference atom *i* and neighbour atom *j*, and if R_{ij} is larger than the cutoff radius (R_c), then the cutoff function is zero. A cutoff of 6.5 Å and total of 53 symmetry functions (Table S1) with different parameters for representing the local atomic environments were used. The neural networks were composed of two hidden layers with 32 and 16 nodes (**Supplementary Section 2**). MD simulation was performed with Large-scale Atomic/Molecular Massively Parallel Simulator (LAMMPS)[43]. The interaction potential of Pt was parametrized by constructed NNP as described in the previous section. Individual Pt NPs were placed in the simulation cell with 15 Å of vacuum space to make the periodic interactions negligible. The cutoff radius of the pair atomic distance was 6.5 Å. After energy minimization of the system using the Polak-Ribiere version of the conjugate gradient (CG) algorithm, the ligand detachment process was simulated for each Pt NC through NVT Nosé–Hoover thermostats, and

atomic configurations of Pt were captured every 0.5 ps. The kMC simulation was performed *via* MonteCoffee[44] with the first reaction method (FRM) algorithm[45]. The scaling relations of adsorption energies for CO oxidation reaction intermediates as a function of GCN were adopted from the previous literature[46]. **Supplementary Section 4** describes the details of the modification of the adsorption energy by atomic strain and the kMC simulation.

Declarations

Acknowledgements

H. C., S. J. H., and B. H. acknowledge the Global Frontier Program through the Global Frontier Hybrid Interface Materials (GFHIM) of the National Research Foundation of Korea (NRF) funded by the Ministry of Science and ICT (Project No. 2013M3A6B1078882) and Creative Materials Discovery Program through the NRF funded by the Ministry of Science and ICT (NRF2017M3D1A1039287). J. K. acknowledges the Ministry of Trade, Industry, and Energy (MOTIE), Korea, under the “Digital manufacturing platform" (No. N0002598) supervised by the Korea Institute for Advancement of Technology (KIAT). H. C. and B. H. K. acknowledge (Project No. NRF- R1C1C11014339). D. K., J. H., and J. P. acknowledge Institute for Basic Science (Project No. IBS-R006-D1) and the National Research Foundation of Korea (NRF) grant funded by the Korea government (MIST) (No. NRF-2020R1A2C2101871, No. NRF-2019M3E6A1064877, and No. NRF-2021M3H4A1A02049904).

References

1. Munnik, P., de Jongh, P. E. & de Jong, K. P. Recent developments in the synthesis of supported catalysts. Chemical reviews **115**, 6687–6718 (2015).
2. Newton, M. A. Dynamic adsorbate/reaction induced structural change of supported metal nanoparticles: heterogeneous catalysis and beyond. Chemical Society Reviews **37**, 2644–2657 (2008).
3. Liu, L. & Corma, A. Identification of the active sites in supported subnanometric metal catalysts. Nature Catalysis **4**, 453–456 (2021).
4. Cargnello, M. *et al.* Efficient removal of organic ligands from supported nanocrystals by fast thermal annealing enables catalytic studies on well-defined active phases. Journal of the American Chemical Society **137**, 6906–6911 (2015).
5. Cargnello, M. *et al.* Control of metal nanocrystal size reveals metal-support interface role for ceria catalysts. Science **341**, 771–773 (2013).
6. Holm, A. *et al.* Nanoscale Spatial Distribution of Supported Nanoparticles Controls Activity and Stability in Powder Catalysts for CO Oxidation and Photocatalytic H2 Evolution. Journal of the American Chemical Society **142**, 14481–14494 (2020).
7. Cargnello, M. Colloidal nanocrystals as building blocks for well-defined heterogeneous catalysts. Chemistry of Materials **31**, 576–596 (2019).

8. Lee, I., Morales, R., Albiter, M. A. & Zaera, F. Synthesis of heterogeneous catalysts with well shaped platinum particles to control reaction selectivity. *Proceedings of the National Academy of Sciences* **105**, 15241–15246 (2008).
9. Núñez, M., Lansford, J. & Vlachos, D. Optimization of the facet structure of transition-metal catalysts applied to the oxygen reduction reaction. Nature chemistry **11**, 449–456 (2019).
10. Huang, W. *et al.* Steam-created grain boundaries for methane C–H activation in palladium catalysts. Science **373**, 1518–1523 (2021).
11. Hu, S. & Li, W.-X. Sabatier principle of metal-support interaction for design of ultrastable metal nanocatalysts. Science **374**, 1360–1365 (2021).
12. Aliaga, C. *et al.* Sum frequency generation and catalytic reaction studies of the removal of organic capping agents from Pt nanoparticles by UV – ozone treatment. The Journal of Physical Chemistry C **113**, 6150–6155 (2009).
13. Lopez-Sanchez, J. A. *et al.* Facile removal of stabilizer-ligands from supported gold nanoparticles. Nature chemistry **3**, 551–556 (2011).
14. Li, D. *et al.* Surfactant removal for colloidal nanoparticles from solution synthesis: the effect on catalytic performance. Acs Catalysis **2**, 1358–1362 (2012).
15. Tahsini, N. *et al.* Colloidal Platinum–Copper Nanocrystal Alloy Catalysts Surpass Platinum in Low-Temperature Propene Combustion. Journal of the American Chemical Society (2022).
16. Pingel, T. N., Jørgensen, M., Yankovich, A. B., Grönbeck, H. & Olsson, E. Influence of atomic site-specific strain on catalytic activity of supported nanoparticles. Nature communications **9**, 1–9 (2018).
17. Ding, K. *et al.* Identification of active sites in CO oxidation and water-gas shift over supported Pt catalysts. Science **350**, 189–192 (2015).
18. Suchorski, Y. *et al.* Resolving multifrequential oscillations and nanoscale interfacet communication in single-particle catalysis. Science **372**, 1314–1318 (2021).
19. Kim, B. H. *et al.* Critical differences in 3D atomic structure of individual ligand-protected nanocrystals in solution. Science **368**, 60–67 (2020).
20. Park, J. *et al.* 3D structure of individual nanocrystals in solution by electron microscopy. Science **349**, 290–295 (2015).
21. Mavrikakis, M., Hammer, B. & Nørskov, J. K. Effect of strain on the reactivity of metal surfaces. Physical Review Letters **81**, 2819 (1998).
22. Liu, P. & Nørskov, J. K. Ligand and ensemble effects in adsorption on alloy surfaces. Physical Chemistry Chemical Physics **3**, 3814–3818 (2001).
23. Li, H., Shin, K. & Henkelman, G. Effects of ensembles, ligand, and strain on adsorbate binding to alloy surfaces. The Journal of chemical physics **149**, 174705 (2018).
24. Calle-Vallejo, F., Loffreda, D., Koper, M. T. & Sautet, P. Introducing structural sensitivity into adsorption–energy scaling relations by means of coordination numbers. Nature chemistry **7**, 403–

410 (2015).

25. Cooper, A. M., Kästner, J., Urban, A. & Artrith, N. Efficient training of ANN potentials by including atomic forces via Taylor expansion and application to water and a transition-metal oxide. npj Computational Materials **6**, 1–14 (2020).
26. Vandermause, J. *et al.* On-the-fly active learning of interpretable Bayesian force fields for atomistic rare events. npj Computational Materials **6**, 1–11 (2020).
27. Tang, L. *et al.* Electrochemical stability of nanometer-scale Pt particles in acidic environments. Journal of the American Chemical Society **132**, 596–600 (2010).
28. Seo, J. K., Khetan, A., Seo, M. H., Kim, H. & Han, B. First-principles thermodynamic study of the electrochemical stability of Pt nanoparticles in fuel cell applications. Journal of power sources **238**, 137–143 (2013).
29. Kim, S. *et al.* Correlating 3D Surface Atomic Structure and Catalytic Activities of Pt Nanocrystals. Nano letters **21**, 1175–1183 (2021).
30. Finney, J. Random packings and the structure of simple liquids. I. The geometry of random close packing. *Proceedings of the Royal Society of London. A. Mathematical and Physical Sciences* **319**, 479–493 (1970).
31. Nilsson Pingel, T., Jørgensen, M., Yankovich, A. B., Grönbeck, H. & Olsson, E. Influence of atomic site-specific strain on catalytic activity of supported nanoparticles. Nature communications **9**, 1–9 (2018).
32. Calle-Vallejo, F. & Bandarenka, A. S. Enabling generalized coordination numbers to describe strain effects. ChemSusChem **11**, 1824–1828 (2018).
33. Lee, K. R. *et al.* In situ manipulation of the d-band center in metals for catalytic activity in CO oxidation. Chemical Communications **57**, 3403–3406 (2021).
34. Yang, A.-C. *et al.* Revealing the structure of a catalytic combustion active-site ensemble combining uniform nanocrystal catalysts and theory insights. *Proceedings of the National Academy of Sciences* **117**, 14721–14729 (2020).
35. Jørgensen, M. & Grönbeck, H. The site-assembly determines catalytic activity of nanoparticles. Angewandte Chemie International Edition **57**, 5086–5089 (2018).
36. Jørgensen, M. & Grönbeck, H. Strain affects CO oxidation on metallic nanoparticles non-linearly. Topics in Catalysis **62**, 660–668 (2019).
37. Kresse, G. & Hafner, J. Ab initio molecular dynamics for liquid metals. Physical Review B **47**, 558 (1993).
38. Kresse, G. & Furthmüller, J. Efficiency of ab-initio total energy calculations for metals and semiconductors using a plane-wave basis set. Computational materials science **6**, 15–50 (1996).
39. Kresse, G. & Furthmüller, J. Efficient iterative schemes for ab initio total-energy calculations using a plane-wave basis set. Physical review B **54**, 11169 (1996).

40. Kresse, G. & Joubert, D. From ultrasoft pseudopotentials to the projector augmented-wave method. Physical review b **59**, 1758 (1999).
41. Behler, J. & Parrinello, M. Generalized neural-network representation of high-dimensional potential-energy surfaces. Physical review letters **98**, 146401 (2007).
42. Khorshidi, A. & Peterson, A. A. Amp: A modular approach to machine learning in atomistic simulations. Computer Physics Communications **207**, 310–324 (2016).
43. Plimpton, S. Fast parallel algorithms for short-range molecular dynamics. Journal of computational physics **117**, 1–19 (1995).
44. Jørgensen, M. & Grönbeck, H. MonteCoffee: A programmable kinetic Monte Carlo framework. The Journal of chemical physics **149**, 114101 (2018).
45. Jansen, A. P. J. *An introduction to kinetic Monte Carlo simulations of surface reactions*. Vol. 856 (Springer, 2012).
46. Jørgensen, M. & Gronbeck, H. Scaling relations and kinetic Monte Carlo simulations to bridge the materials gap in heterogeneous catalysis. ACS Catalysis **7**, 5054–5061 (2017).

Figures

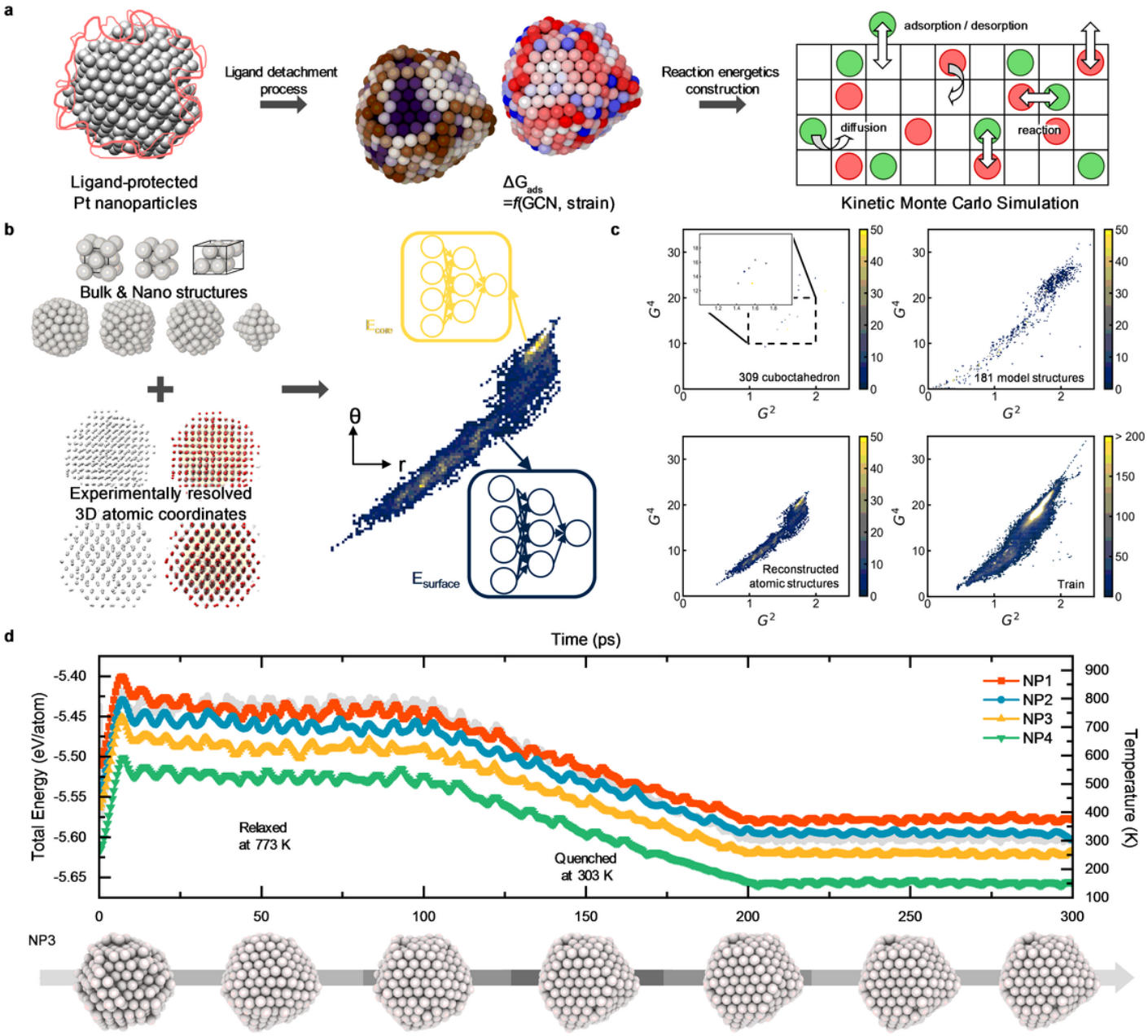

Figure 1

Atomic structure analysis of individual Pt NPs under thermal treatment to remove ligands. a, Schematic illustration of the workflow of individual particle reactivity analysis for ligand-protected Pt NPs. **b**, Illustration of the first-principles data generation strategy, enlarging the number of data points with different local atomic environments. **c**, G^4 and G^2 values of first-principles data for different types of systems. Symmetry function values **θ** (G^4) and **r** (G^2) represent the bond angle and length based on the centre atom, respectively, and they are summed over the neighbouring atoms of the centred atom, where the parameters of each function are as follows: eta: 0.005, zeta: 2, and gamma: 1 for G^4, eta: 8 for G^2. **d**, Temporal changes in the total energy for different size Pt NPs (NP1-NP4) and the temperature (grey line). Below is the temporal structural change of NP3 every 50 ps.

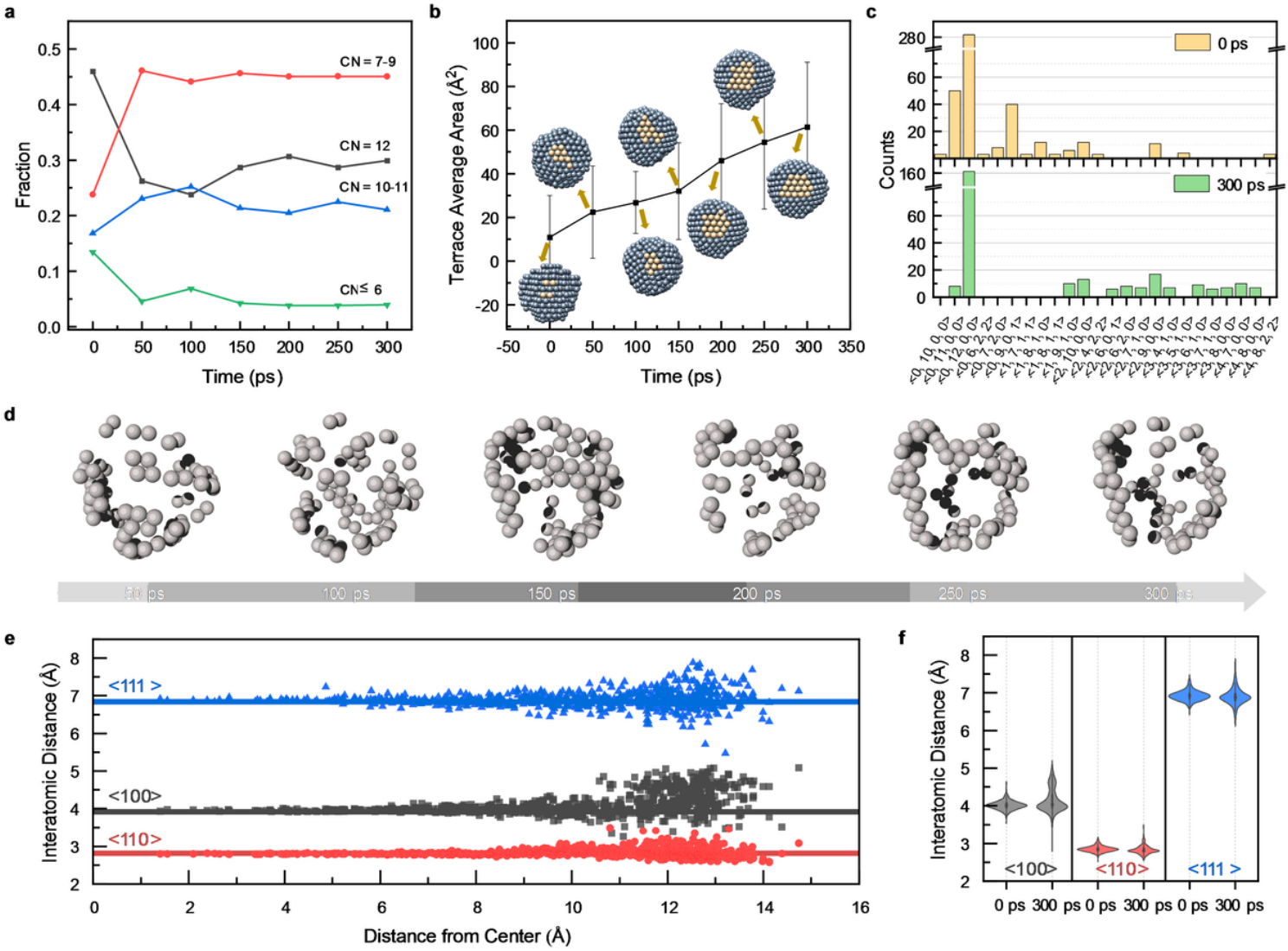

Figure 2

Structural analysis of NP3 during the ligand detachment process. a, Changes in the fractions of CN. **b**, Temporal change in the averaged surface area of eight {111} terraces. The inset figures represent a terrace with yellow. **c**, Most abundant VPs at 0 ps (top) and 300 ps (bottom) in the MD simulation. **d**, Illustration of the change in defective atoms according to Wigner-Seitz defect analysis. **e**, Interatomic distances according to the distance from the centre after the 300 ps MD simulation in the directions of <111>, <100>, and <110> and **f**, violin distribution plots of the interatomic distances at 0 and 300 ps.

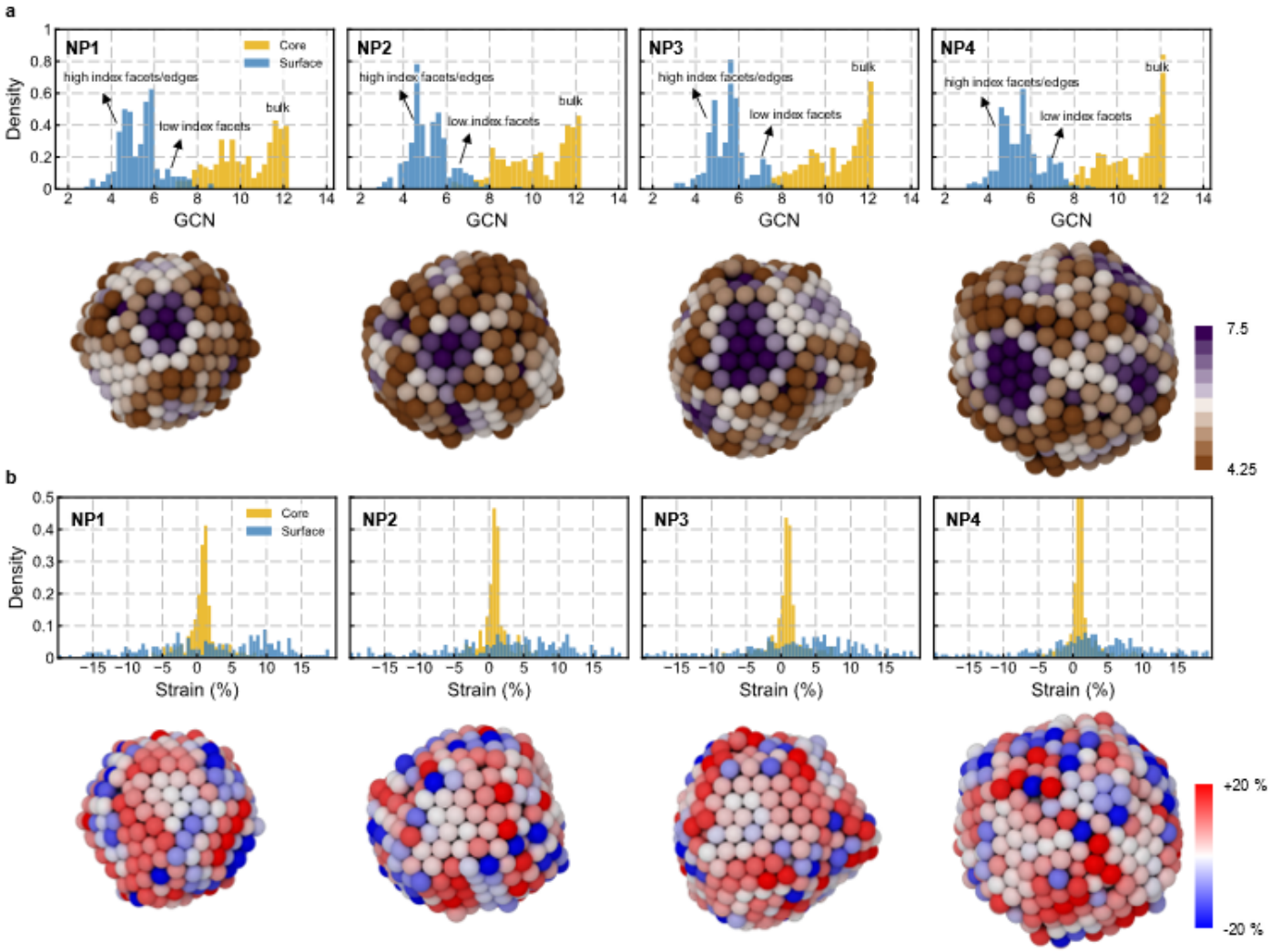

Figure 3

Surface structure analysis of individual Pt NPs after the thermal treatment process. a, GCN distribution of core and surface atoms for Pt NPs after the 300 ps MD simulation (top), and colour-coded GCNs of surface atoms for Pt NPs. **b,** Strain distribution of core and surface atoms for Pt NPs after the 300 ps MD simulation (top), and colour-coded strain of surface atoms for Pt NPs.

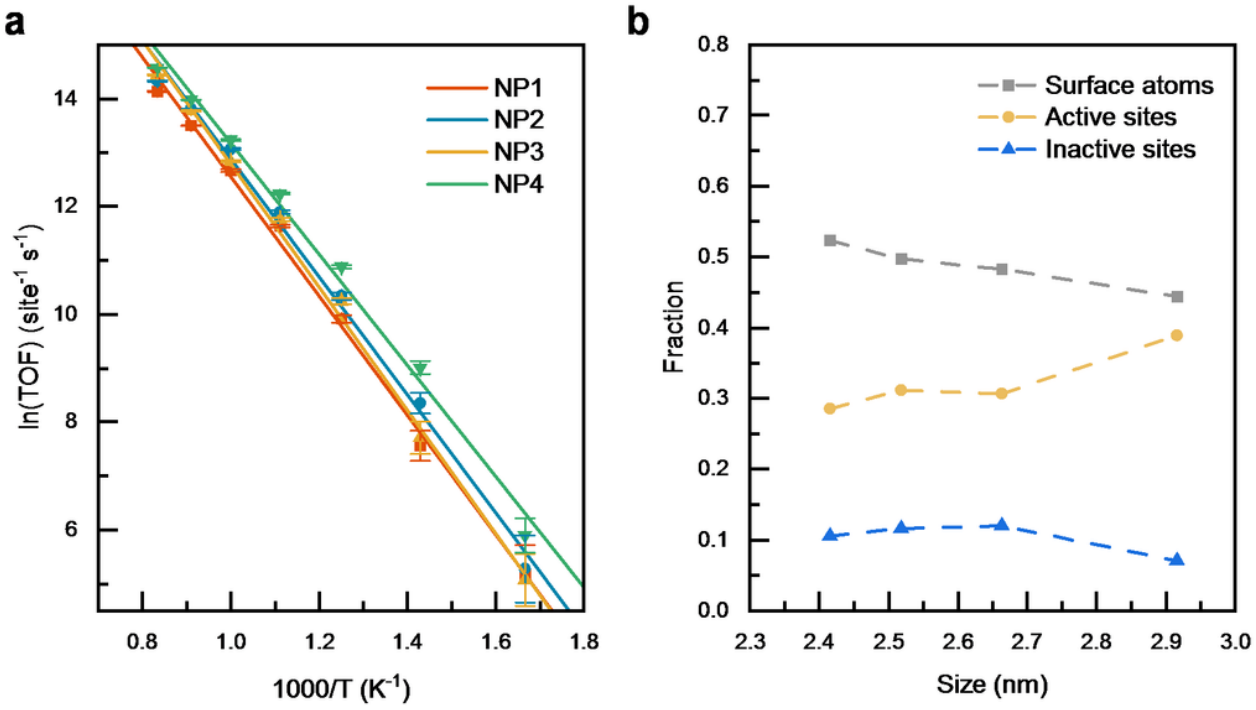

Figure 4

Activity prediction by kMC simulation of Pt NPs. a, Arrhenius plot of the catalytic TOF for different size Pt NPs (NP1-NP4). The error bars represent the standard deviation among fifteen identically prepared simulations. **b,** Atomic fractions of surface atoms and catalytically active and inactive sites at 900 K. The kMC was conducted at fixed pressures (20 mbar CO and 10 mbar O_2).

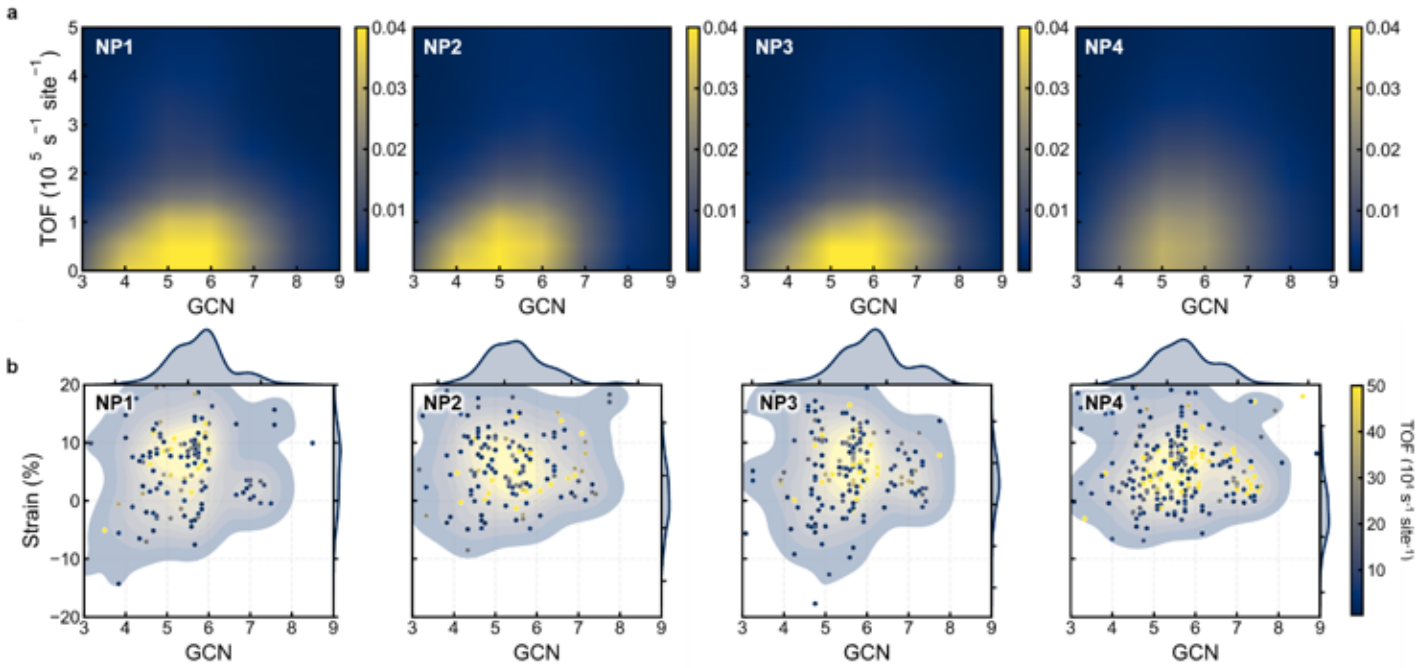

Figure 5

Individual active site contributions to the TOF at 900 K. a, Colour density maps of TOF *vs.* GCN for different Pt NPs (NP1-NP4). **b**, Distribution of geometric effects for individual sites (strain and GCN) on the TOF.

Supplementary Files

This is a list of supplementary files associated with this preprint. Click to download.

- SIsubmission.docx
- floatimage1.jpeg